

Nitrogen-Vacancy Magnetometry of Edge Magnetism in WS₂ Flakes

Ilja Fescenko^{1,&,} Raman Kumar,^{2,&} Thitinun Gas-Osoth,^{3,4,5,&} Yifei Wang,^{3,4,&} Suvechhya Lamichhane,⁶ Tianlin Li,⁶ Adam Erickson,³ Nina Raghavan,⁶ Tom Delord,² Cory D. Cress,⁷ Nicholas Proscia,⁷ Samuel W. LaGasse,^{7,8} Sy-Hwang Liou,⁶ Xia Hong,⁶ Jose J. Fonesca,⁷ Toshu An,⁴ Carlos A. Meriles,^{2,*} and Abdelghani Laraoui^{3,6,*}*

¹Laser Center, University of Latvia, Jelgavas St 3, Riga, LV-1004, Latvia

²Department of Physics, CUNY-City College of New York, 85 St. Nicholas Terrace, New York, NY 10031, USA

³Department of Mechanical & Materials Engineering, University of Nebraska-Lincoln, 900 N 16th St, W342 NH, Lincoln, NE 68588, USA

⁴Japan Advanced Institute of Science and Technology, 1-1 Asahidai, Nomi, Ishikawa 923-1292, Japan

⁵Present address: School of Science, Department of Physics, University of Phayao, 19 Moo 2, Tambon Maeka, Mae Ka, Phayao 56000, Thailand

⁶Department of Physics and Astronomy and the Nebraska Center for Materials and Nanoscience, University of Nebraska-Lincoln, 855 N 16th St, Lincoln, NE 68588, USA

⁷Electronics Science and Technology Division, US Naval Research Laboratory, 4555 Overlook Ave SW, Washington, DC 20375, USA

⁸Laboratory for Physical Sciences, 8050 Greenmead Drive, College Park, MD 20740

&Equal contributions

*Corresponding Authors: iliafes@gmail.com, cmeriles@ccny.cuny.edu, alaraoui2@unl.edu

Abstract

Two-dimensional (2D) magnets are of significant interest both as a platform for exploring novel fundamental physics and for their potential applications in spintronic and optoelectronic devices. Recent magnetic bulk measurements have indicated a weak ferromagnetic response in WS₂ and theoretical predictions suggest that the edges of such flakes exhibit magnetization when at least one edge of a flake is partially hydrogenated. Here, we use room-temperature wide-field quantum diamond magnetometry to image pristine and Fe-implanted WS₂ thin flakes of variable thickness, exfoliated from a bulk crystal and transferred to nitrogen-vacancy (NV)-doped diamond substrates. We provide the first direct evidence of edge-localized stray fields, growing linearly with the applied magnetic field and reaching up to ± 4.7 μ T. Magnetic simulations using alternative models favor the presence of edge magnetization aligned along an axis slightly tilted from the normal to the WS₂ flake's plane. Our observations open intriguing opportunities on the use of WS₂ for spintronics applications.

1. Introduction

The recent discovery of two-dimensional (2D) magnetism^[1-5] has garnered significant interest, as the ability to stack atomic layers of different magnetic materials or the same material with varying relative orientations offers countless opportunities for both fundamental and applied research. Particularly promising among these applications are spin-based technologies, such as energy-efficient memories,^[6] non-volatile memristive devices,^[7] and random number generators,^[8] systems that have traditionally relied on dilute magnetic semiconductors. Significant progress has

been made in characterizing and understanding the ferromagnetic properties of Cr- and Fe-based 2D systems,^[9,10] but their metallic or insulating properties hinder seamless device integration due to challenges in electrical compatibility and interface engineering.^[11]

To address these limitations, substantial efforts have been dedicated to investigating transition-metal dichalcogenides (TMDs) such as MoSe₂, MoS₂, and VSe₂,^[12–16] where first-principles calculations predicted room-temperature ferromagnetism down to the monolayer level when doped with Fe, Co, or Mn.^[9,17,18] Experimental studies have largely confirmed these predictions, demonstrating ferromagnetism in few-layer TMD flakes containing various dopants. In addition to those mentioned above,^[19,20] the list has expanded to include V,^[16,21] Ni,^[22] Cu,^[23] and Nb.^[20]

Tungsten disulfide (WS₂), another member of the TMD family, has primarily garnered attention for optoelectronic applications for its tunable bandgap, which changes from indirect to direct when transitioning from bulk to monolayer form (~ 2 eV).^[24,25] Recent bulk vibrating sample magnetometer (VSM) and superconducting quantum interference device (SQUID) measurements of pristine WS₂ nanosheets showed intrinsic room-temperature ferromagnetism,^[26,27] hence extending the range of potential applications to spintronics.

The origin of ferromagnetism in WS₂ nanostructures remains, however, not fully understood. *Ab initio* calculations suggest the presence of spin-polarized edge states along the zigzag edges of WS₂ flakes, even in the absence of externally applied magnetic fields.^[28] SQUID magnetometry measurements on WS₂ nanosheets reveal a ferromagnetic-like hysteresis, whereas bulk WS₂ does not exhibit such behavior.^[26,27] A separate study showed ferromagnetism in Fe:MoS₂ but not in Fe:WS₂, which was attributed to the formation of deep level traps.^[29]

Despite these preceding studies, the local magnetic properties of pristine or doped thin WS₂ flakes and sheets remain underexplored, primarily due to the lack of characterization methods featuring suitable spatial resolution and magnetic sensitivity. To circumvent this problem, the last decade has witnessed a sustained effort aimed at the use of color centers as local magnetic probes. A particularly successful example is the nitrogen-vacancy (NV) center in diamond, a paramagnetic defect whose spin can be initialized and readout optically.^[30–32] NV-based optically detected magnetic resonance (ODMR) has now evolved to allow the detection of weak magnetic fields with nanometer-scale spatial resolution, thereby offering new opportunities for investigating the magnetic properties of thin films^[33–37] and 2D materials.^[38–41] We note that other techniques such as magneto-optical Kerr effect microscopy (MOKE)^[1,2] and magnetic force microscopy (MFM)^[23,42] have been previously applied to investigating 2D magnets. However, the use of NV magnetometry offers superior magnetic sensitivity and/or spatial resolution, much needed to study the magnetic properties of these systems under ambient conditions.^[32,38,39,43–45]

Here, we investigate the room-temperature magnetic response of pristine and Fe implanted WS₂ flakes under a varying magnetic field. In our experiments, we transferred pristine and Fe implanted WS₂ flakes onto diamond films engineered to host an ensemble of near-surface (~ 6 – 150 nm) NV centers. NV stray-field imaging of individual flakes featuring varying thickness revealed clear magnetic signatures in both pristine and Fe-implanted WS₂, which allowed us to examine five different models of magnetization.^[26,28] Our results provide the first direct evidence of edge-localized magnetism in WS₂ flakes, revealing its amplitude, orientation, and spatial distribution.

2. Results and Discussion

2.1. NV magnetometry of pristine WS₂ flakes

Our experiments leverage advances on the use of NV centers in diamond as local magnetic probes

(see Methods for detailed discussion). The NV center is formed by a substitutional nitrogen adjacent to a vacancy and features a ground state spin triplet whose relative populations can be optically read out utilizing spin-selective intersystem crossing to a singlet manifold^[46] (Figure 1a). Figure 1b shows a schematic of the NV widefield microscope.^[30,31] We optically excite the NVs via a green laser (130 mW, 532 nm), and collect the NV fluorescence (650 – 800 nm) via a sCMOS camera (Supporting Information, Section S2). We position the diamond above a glass coverslip patterned with Ti /Cu thick striplines (respectively 5 nm and 1.5 μm thick) for microwave (MW) manipulation of the NV spin states. A magnetic field is applied along the [111] orientation for both (100) and (110) oriented diamonds (Figure 1c).^[25,26,34] When magnetized, the WS₂ flake (Figure 1d) generates a stray magnetic field B_{str} along the NV axis, which leads to a change in the effective magnetic field $B_{eff} = B_{app} + B_{str}$ acting on the NVs, thus altering the f_{-1} ($|0\rangle \leftrightarrow |-1\rangle$) and f_{+1} ($|0\rangle \leftrightarrow |+1\rangle$) NV spin transition frequencies.^[30,31] Figure 1e depicts the NV ODMR resonances in the (100) diamond at $B_{app} = 63.2$ mT, fitted with a Lorentzian to determine f_{-} and f_{+} . We transferred three pristine and one Fe-implanted WS₂ flakes — thereafter referred to as Flakes 1, 2, 3, and 4, these were deposited on diamond substrates cut and polished along the (100) plane for Flakes 1 and 3, and the (110) plane for Flake 2 and Flake 4. In all diamonds, we align B_{app} along the NV crystalline [111] axis corresponding to angles $(\theta_{NV}, \varphi_{NV})$ of $(54.7^\circ, 90^\circ)$ and $(90^\circ, 0^\circ)$ for the (100) and (110) planes, respectively (Figure 1c).

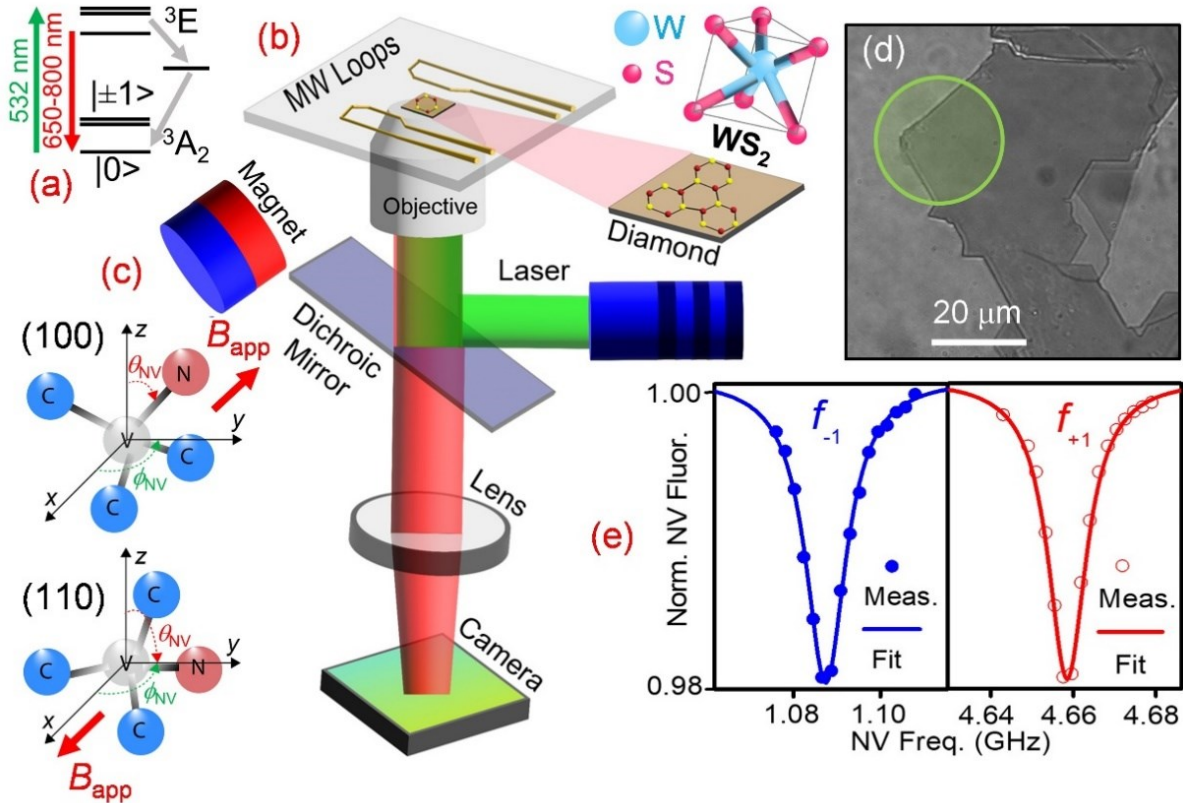


Figure 1. (a) Schematic of the NV center electronic energy levels. (b) ODMR widefield microscope setup. The inset of (b) illustrates the WS₂ unit cell. (c) Relative NV axis orientations for (100) and (110) diamonds used in this study (top and bottom, respectively). (d) Optical image of a WS₂ Flake 1 on a (100) diamond surface; the green circle marks the area illuminated during measurements. (e) NV ODMR spectrum in the (100) diamond at a magnetic field of 63.2 mT aligned along the NV [111] axis.

Figures 2(a-c) show B_{str} maps from a region of pristine Flake 1 (thickness of 160 nm, measured by atomic force microscopy (AFM) in Figure S1.4, Supporting Information) for applied magnetic fields of 4.4, 39.6, and 63.2 mT, respectively. We find the NV signal can have positive or negative signs on different edges as clearly seen in Figure 2c. To evaluate the magnetic response, we make line cuts of the measured B_{str} at the flake edges, as indicated by the red and blue dashed lines, and plot them separately in Figures 2d and 2e. We define the stray field strength ΔB as a peak-to-peak amplitude between the maximum and minimum in the B_{str} signal.^[30,31] The absolute value of ΔB increases from $0.75 \pm 0.3 \mu\text{T}$ at 4.4 mT to $4.7 \pm 0.3 \mu\text{T}$ at 63.2 mT. As seen in Figure 2f, the stray field amplitude grows linearly with the applied magnetic field, indicative of weakly ferromagnetic^[29] or paramagnetic^[30,31] behaviors, discussed below.

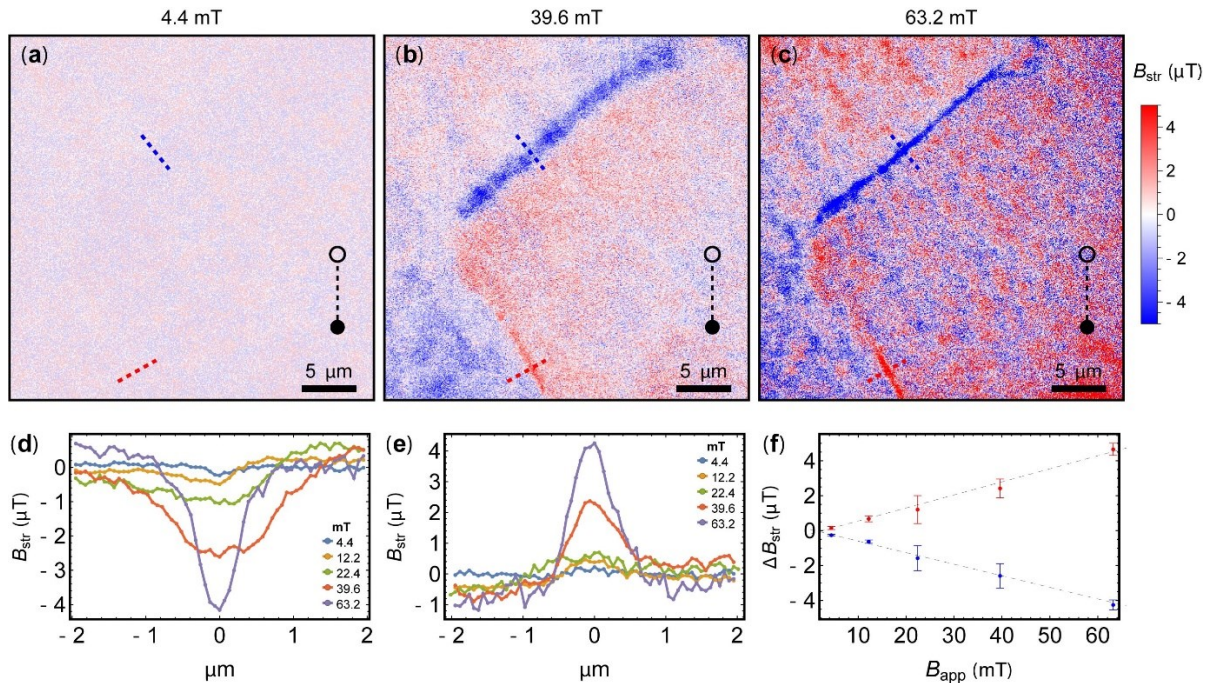


Figure 2. (a-c) NV B_{str} maps of a WS₂ Flake 1 under an applied magnetic field B_{app} of 4.4 mT, 39.6 mT, and 63.2 mT, respectively. The black dashed line with circles indicates the NV axis projection on the image x-y plane. (d-e) Line cuts of B_{str} across the WS₂ flake edges, corresponding to the blue and red dashed lines in (a-c), revealing field variations at different applied magnetic fields. (f) Magnetic shift ΔB_{str} extracted from (d-e) as a function of B_{app} ; the dashed lines are linear fits.

Figures 3b and 3e display the measured B_{str} from Flake 1 and Flake 2 (thickness of ~ 100 nm): Unlike the “absorptive” stray field profile seen for Flake 1, Flake 2 exhibits a “dispersive” shape, which is a consequence of the varying relative orientations of the NV axis and the flake magnetization at a given edge.

To quantitatively interpret these patterns, we perform three-dimensional magnetostatic modeling using finite-element analysis (COMSOL Multiphysics), see Supporting Information Section S4 and Figure S4. Figure 3c and Figure 3f show the calculated stray magnetic field in either case. These edge patterns are a result of projecting B_{str} along the NV axes corresponding to each diamond orientation (i.e., along a 54.7° out-of-plane vector in the (100) diamond and in-plane for the (110) case). To investigate the nature of magnetism in WS₂, we consider five distinct magnetization geometries (subsequently referred to as models). Comparison of the measured data

with simulations allow us to determine the most likely magnetization model, irrespective of preceding theoretical expectations. Specifically, for each model, we simulated profiles along the dashed lines shown in Figure 3b and Figure 3e, fitting their amplitudes to the measured stray field profiles. The upper rows of Figure 4a and Figure 4b schematically illustrate the geometries of the tested models. The blue arrows indicate the applied magnetic field, consistently aligned along the NV [111] axis, as depicted by a dumbbell drawing. The brown arrows represent uncompensated spins responsible for magnetization.

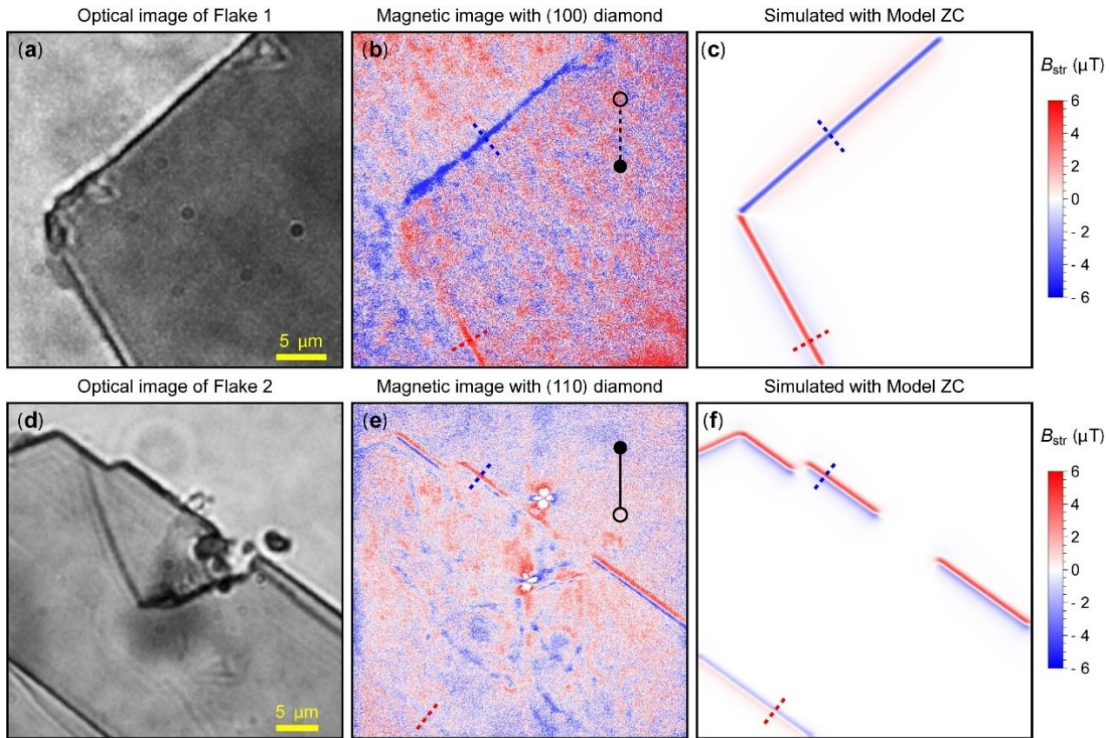


Figure 3: Optical images of WS₂ Flake 1 (a) and Flake 2 (d) on diamond substrates. Stray field magnetic images acquired at B_{app} of 63.2 mT and 220 mT of Flake 1 (b) and Flake 2 (e) transferred to (100) and (110) diamond, respectively. The applied magnetic field is aligned along the diamond [111] axis. The black lines with circles represent the NV axis projection in the image plane. Simulated stray field maps of Flake 1 (c) and Flake 2 (f) using Model ZC, which assumes edge magnetization along the z-axis normal to the image plane.

Figure 4 compares the experimental NV magnetometry profile with simulated results for five different magnetic states. In Model P (Paramagnetic), we assume that the entire flake is paramagnetically magnetized in the applied field, whereas in Model PE (Paramagnetic Edge), only the edges exhibit paramagnetic behavior. We model edge magnetization by assigning a uniform volume magnetization to a bar with a cross-section of 200 nm (width) \times 300 nm (height), placed along the edge of an otherwise non-magnetized flake. In Figure 3 and Figure 4, the best-fit volume magnetizations are 50 A/m for Flake 1 and 80 A/m for Flake 2. Given the applied magnetic fields of 63.2 mT and 220 mT, respectively, the higher value for Flake 2 likely corresponds to a saturated magnetization state. To estimate the magnetic moment associated with the edge, one must convert the modeled volume magnetization using the ratio between the cross-section of the model bar and the actual magnetized volume, which is approximately given by the flake height multiplied by the in-plane lattice constant. To account for the limited spatial resolution, the simulated magnetic

image was convolved with a Gaussian kernel of 325 nm, effectively smoothing sharp field gradients at the bar edges. The finite cross-section of the bar has negligible influence on the resulting field profile and serves as a reasonable approximation of an edge-localized magnetization in our wide-field NV microscope. This microscope operates at diffraction-limited resolution, detecting fluorescence at wavelengths >650 nm^[30,31] and thus any spin volume smaller than approximately half the detection wavelength appears spatially broadened into a diffraction-limited spot. The assumption that the magnetized region of the WS₂ flakes is smaller than the diffraction-limited spot is supported by the observation that the widths of the stray-field signals remain consistent across all measurements (Figures 2–5).

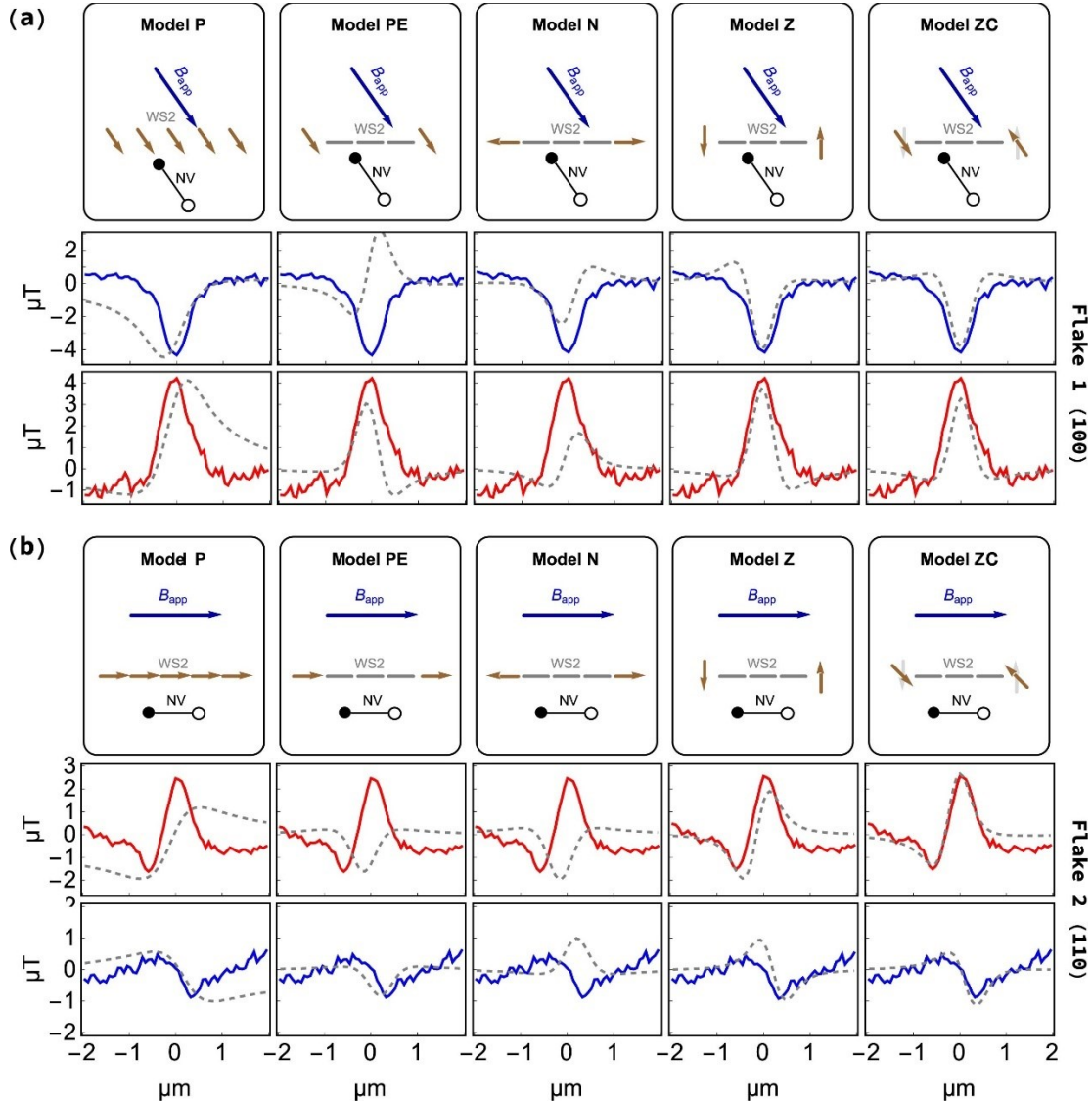


Figure 4: Comparison of simulated and experimental NV magnetometry profiles for WS₂ Flake 1 (a) and Flake 2 (b) with different edge magnetization configurations. The top (a, Flake 1) and bottom (b, Flake 2) panels illustrate simulations for distinct magnetization geometries of WS₂ edges under an applied magnetic field B_{app} . The experimental data (solid red and blue lines) correspond to NV magnetometry profiles measured along opposite edges of WS₂ flakes. Simulated profiles (dashed gray lines) in (a-b) are overlaid for direct comparison.

In Model N (Normal), we assume that uncompensated magnetic moments are oriented perpendicular to the edge faces of the flakes, forming a 90-degree angle with the side faces, while Model Z posits that the magnetic moments are aligned along the z -direction, normal to the imaging and flake's plane. Drawing on References [26,28] and our experimental observations, we propose that the magnetic moments could be oriented either along or opposite to the z -axis.

While the first three models (P, PE, and N) significantly depart from the measured data (see bottom rows of Figure 4a and Figure 4b), Model Z shows instead good agreement across both geometries. To address minor inconsistencies — such as the slightly asymmetric dispersive experimental profile in Figure 4b or the lack of asymmetry in the experimental profiles in Figure 4a — we introduce the angle between the z -axis and the magnetization (in the yz plane) as a fitting parameter. The resulting fit, shown in Figure 4 as Model ZC (Z Canting), is attributed to spin canting in antiferromagnets, where magnetic moments deviate from perfect antiparallel alignment due to external magnetic fields, Dzyaloshinskii–Moriya interactions, or crystal anisotropy, resulting in a small net magnetic moment.^[47]

The observed positive and negative stray-field features consistently exhibit similar amplitudes, which does not fully align with theoretical predictions^[29] suggesting that different atomic species in monolayer WS₂ (i.e., S and W atoms) contribute unequally to the local magnetic moment. However, when comparing different flakes, the amplitudes of the magnetic signals show a rather small dependence on flake thickness. Pristine Flake 3 (thickness of 45 nm from AFM in Figure S1.4) exhibits a smaller magnetic signal compared to Flake 1 (thickness of 160 nm) under the same applied field of 63.2 mT (see Figure S3.3). The reduction in signal amplitude is only about a factor of two, while the difference in spatial width is masked by the diffraction-limited resolution. This relatively modest amplitude change is expected: while a thicker edge contains more dipoles, the stray magnetic field decays as $1/r^3$, meaning that dipoles farther from the NV plane contribute less. For flakes of 45 nm and 160 nm thickness, simulations predict a difference in stray field amplitude of less than 2%. Therefore, the observed measured difference is most likely due to a slightly larger NV–sample standoff for Flake 3 compared to Flake 1. We note that we used a hexagonal boron nitride (hBN) flake (thickness of ~100 nm) to cap the thin WS₂ Flake 3 and prevent contamination/oxidation. As shown in Figure S3.3a in Supporting Information, this led to an increase of fluorescence (~2 times higher than the NV fluorescence) from unpolarized green excitation at the edges between hBN and WS₂ flakes, that may be explained by the activation of other quantum emitters as a result of carrier trapping in deformation potential wells localized near the edges between hBN and WS₂,^[48] or by waveguiding effects induced by hBN.^[49] This extra fluorescence can affect the NV ODMR contrast in Flake 3 in comparison to Flake 1 (no hBN) at the same laser power (130 mW) and averaging time (10 seconds per frame).

2.2. NV magnetometry of Fe-implanted WS₂ flakes

We have also conducted NV measurements on selected Fe-implanted (energy of 30 eV, dose of $10^{13} - 10^{14}$ Fe⁺/cm²) WS₂ flakes transferred onto (110) diamond, as shown in Figure 5a. More information about Fe⁺ beam implantation is provided in Supporting Information Section S1. Figure 5b and Figure 5c respectively present the measured and simulated B_{str} maps at an applied field of 182 mT, corresponding to a region highlighted by circles in Figure S1.2. The profiles along the dashed lines were fitted to simulated profiles using Model ZC, as depicted in Figure 5c. The width and shape of these profiles (Figure 5d) resemble those of pristine flakes (similar Flake 2 transferred into (110) diamond), though no evidence of uniform magnetization due to Fe implantation was observed across the flake. This suggests that magnetism in WS₂ flakes originates most likely from

the flake edges^[26,28] or other local defects present in the material,^[50] rather than the Fe doping.^[29] This behavior is confirmed from previous bulk measurements on WS₂ powder, in which the magnetization is enhanced by increasing the annealing temperature up to 700 °C and therefore increasing the edge defects density, confirmed from X-ray photoelectron and electron paramagnetic resonance spectroscopies.^[50] Nevertheless, the low energy Fe⁺ shallow (~1 – 3 nm) implant without annealing, may not be enough to activate Fe centers within the WS₂ flakes. Future studies on flakes exposed to varying dose and implantation energy of Fe⁺ ions may show a measurable response in the Fe-implanted WS₂ flakes.

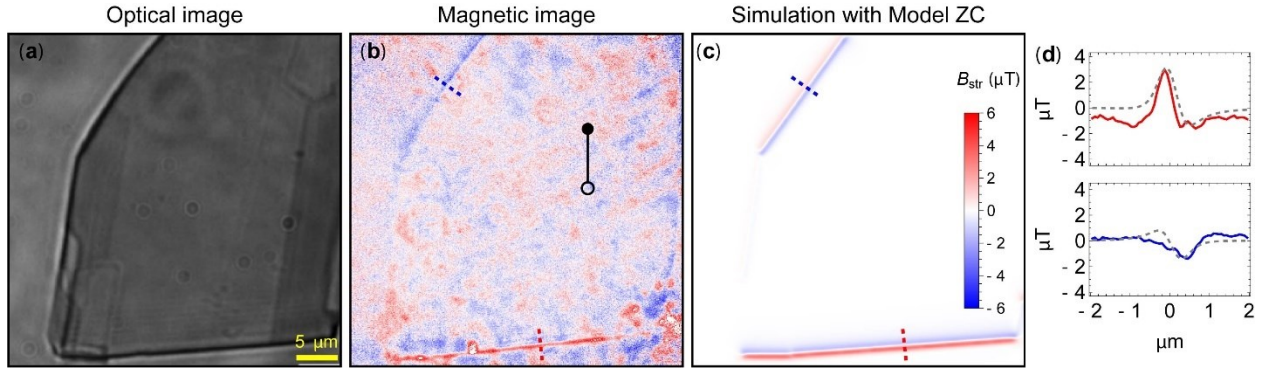


Figure 5. Optical image (a), measured (b), and simulated stray field map using Model ZC (c) which assumes edge magnetization along the z -axis normal to the image plane with weak paramagnetic behavior. The experimental data (solid red in d and blue lines in e) correspond to NV magnetometry profiles measured along opposite edges of WS₂ flake in (b). Simulated profiles (dashed gray lines) in (d) are overlaid for direct comparison.

3. Conclusion

To conclude, we have employed wide-field NV magnetometry to map the room-temperature magnetic stray fields of pristine and Fe-implanted WS₂ flakes (45–160 nm thick) transferred onto (100) and (110) diamond substrates. Our measurements reveal distinct magnetic signatures localized at the flake edges, with stray fields up to ± 4.7 μT that scale linearly with the applied magnetic field (4.4–220 mT). By comparing experimental data with finite-element simulations across five magnetization models, we have found that the observed profiles can be best described by edge-localized magnetization slightly tilted from the z -axis. This tilt suggests a complex interplay between intrinsic edge magnetism and the applied magnetic field, partially deviating from theoretical predictions of purely z -aligned spin-polarized edge states.

Notably, Fe-implanted flakes exhibit edge magnetism similar to pristine flakes, with no evidence of uniform magnetization induced by doping, supporting the hypothesis that magnetism in WS₂ originates primarily from zigzag edge defects rather than dopants. The modest dependence of stray field amplitude on flake thickness (e.g., ~ 2 -fold reduction from 160 nm to 45 nm) aligns with the $1/r^3$ decay of dipole fields, where thicker edges contribute more dipoles, but distant ones have diminished impact at the NV sensing plane (~ 6 –150 nm standoff).

These findings provide direct evidence of edge-localized ferromagnetism in WS₂ flakes at room temperature, advancing our understanding of 2D magnetism in transition metal dichalcogenides. The ability to probe nanoscale magnetic features with NV magnetometry highlights its potential as a tool for characterizing 2D magnets with high sensitivity and spatial

resolution.^[32,42] However, the limited spatial resolution (~ 325 nm) of wide-field NV microscopy obscures finer details of edge magnetization, and the exact nature of the observed tilt in the ZC model remains unclear, potentially reflecting external or internal field effects.

Future studies could leverage NV-scanning probe microscopy^[32,38,51] (~ 50 nm resolution) with NV ensembles to resolve sub-edge magnetic structures with weak magnetic stray fields and exfoliate monolayer WS₂ flakes to explore ferromagnetic order at the atomic limit. Such efforts could enable WS₂-based spintronic devices,^[52] such as magnetic tunnel junctions or spin valves, by harnessing edge magnetism. Additionally, combining NV magnetometry with complementary techniques (e.g., MOKE)^[32,42] could clarify the interplay between edge and bulk contributions, further elucidating the mechanisms of ferromagnetism in WS₂ and related TMDs. In a recent theory study, it was found that the edge magnetism in TMDs depends highly on the edge filling of electronic states.^[53] Therefore, a modulation (e.g., electrical) of the edge magnetic phases could be experimentally observed in gated TMD samples including WS₂.

4. Methods

Samples preparation: WS₂ flakes with a thickness of 45–160 nm were prepared by mechanical exfoliation from a bulk WS₂ crystal (HQ Graphene) onto a 100 nm SiO₂/Si substrate with pre-patterned etched marks, see Supporting Information, Figure S1.1. After thermal annealing, we used shadow masks and Fe implantation to create doped areas in some of the flakes (see Supporting Information Section S1 for further details). Then, select WS₂ flakes were picked up from SiO₂/Si and Au/Ti-coated SiO₂/Si substrates and transferred onto NV doped diamond using high-temperature dry transfer^[54,55] with polypropylene carbonate (PPC) stamps. Thicker WS₂ flakes were transferred directly using PPC (Figure S1.3(a-c)), while we added a protective top layer of hBN on PPC for thinner flakes (Figure S1.3(d-f)). To release the flakes onto the diamond, the PPC stamp was brought into contact with the substrate at 60 °C; the samples were then heated to 100 °C to fully melt the PPC, allowing the flakes to detach. The flakes' thickness is retrieved from atomic force microscopy and by correlating it with the flakes color using optical microscopy measurements, see Figure S1.1b.

NV Magnetometry: In this study, we used ¹⁵N implantation^[31,34,56] to create ~ 6 -nm^[34,56] and ~ 150 -nm^[30,31] thick NV sensing layers into two $2 \times 1 \times 0.08$ mm³ electronic grade (100) and (110) diamonds (see Supporting Information Section S2 and Figure S2(a-b) for more details on NV creation). For NV measurements, we first locate the WS₂ flake of interest with the help of a sCMOS camera and then record the ODMR signal by steering the NV fluorescence into an avalanche photodetector connected to a Yokogawa oscilloscope. To map the stray field emanating from the WS₂ flakes, we collect the NV fluorescence at each MW frequency by the sCMOS camera (for a total of 16 frames per spin transition), we then evaluate the ODMR dips at each pixel using an amplitude-weighted mean method,^[57] as shown in Figure 1e. We calculate B_{str} from the formula:^[30,31]

$$B_{str} = (f_+ \pm f_-)/2\gamma_{NV} - B_{app} \quad (1)$$

where $\gamma_{NV} = 28$ GHz/T is the gyromagnetic ratio of the NV electron spin, and we use the minus (plus) sign for $B_{app} < 102.5$ mT ($B_{app} > 102.5$ mT), take into account the ground-state spin level anti-crossing. This strategy allows us to remove any background signal coming from local strain and thermal effects leaving only the stray magnetic field produced by the WS₂ flakes.^[30,31]

Acknowledgements

I.F. acknowledges support from the Latvian Quantum Initiative under European Union Recovery and Resilience Facility project no. (2.3.1.1.i.0/1/22/I/CFLA/001). A.L., S.-H.L., and X.H. acknowledge the National Science Foundation (NSF) through EPSCoR RII Track-1: Emergent Quantum Materials and Technologies (EQUATE) Award OIA-2044049. A.L. and X.H. acknowledge the University of Nebraska-Lincoln (UNL) Grand Challenges catalyst award entitled “Quantum Approaches addressing Global Threats”. A.L. acknowledges additional support from NSF Award 2328822. C.A.M. acknowledge support from NSF Award 2203904 and from the Department of Defense Award DOD-W911NF-25-1-0134. The research done at UNL was performed in part in the Nebraska Nanoscale Facility: National Nanotechnology Coordinated Infrastructure and the Nebraska Center for Materials and Nanoscience (and/or NERCF), supported by NSF Award 2025298. R.K., T.D. and C.A.M. acknowledge access to the facilities and research infrastructure of the NSF CREST IDEALS, Award 2112550.

Conflict of Interest

The authors declare no conflict of interest.

Author Contributions

I.F., J.J.F., C.A.M., and A.L. designed the experiment and supervised the project. T.G.-O., Y.W., and T.A. performed NV measurements and analyzed the data, with assistance from S.L., S.-H.L., I.F., and A.L. C.D.C, N.P., S.W.L., and J.J.F. synthesized the WS₂ flakes, conducted optical and atomic force microscopy characterization, exfoliated the WS₂ flakes onto a SiO₂/Si substrate, and performed Fe⁺ implantation on selected WS₂ flakes. R.K. and T.D. conducted COMSOL simulations of magnetic stray fields. T.L., N.R., and X.H. transferred WS₂ flakes onto the diamond using PPC and/or hBN methods. A.E. conducted additional atomic force microscopy characterization on select WS₂ flakes. I.F. performed the fitting using distinct magnetization models. I.F., R.K., C.A.M., and A.L. wrote the manuscript, with contributions and feedback from all authors.

Data Availability Statement

The data that support the findings of this study are available from the corresponding author upon reasonable request.

Keywords

nitrogen-vacancy, magnetometry, WS₂, transition metal dichalcogenide, magnetism.

Supporting Information

S1. Synthesis and characterization of WS₂ (pristine and Fe-implanted) flakes

For our experiments, we used a bulk tungsten disulfide (WS₂) single crystal purchased from HQ Graphene. We generated flakes via physical exfoliation and transfer. The substrate was kept at 80°C during the process to improve WS₂ flake transfer. Desired flake thicknesses ranging from 8 – 340 nm were preselected via optical contrast and atomic force microscopy (AFM), see Figure S1.1(b). Following flake transfer, samples were annealed at 300°C for 1hr in H₂/Ar environment to improve surface cleanness. Selected WS₂ flakes were identified optically, with thickness characterized by atomic force microscopy (AFM, Bruker Dimension FastSCAN), see Figure S1.1.

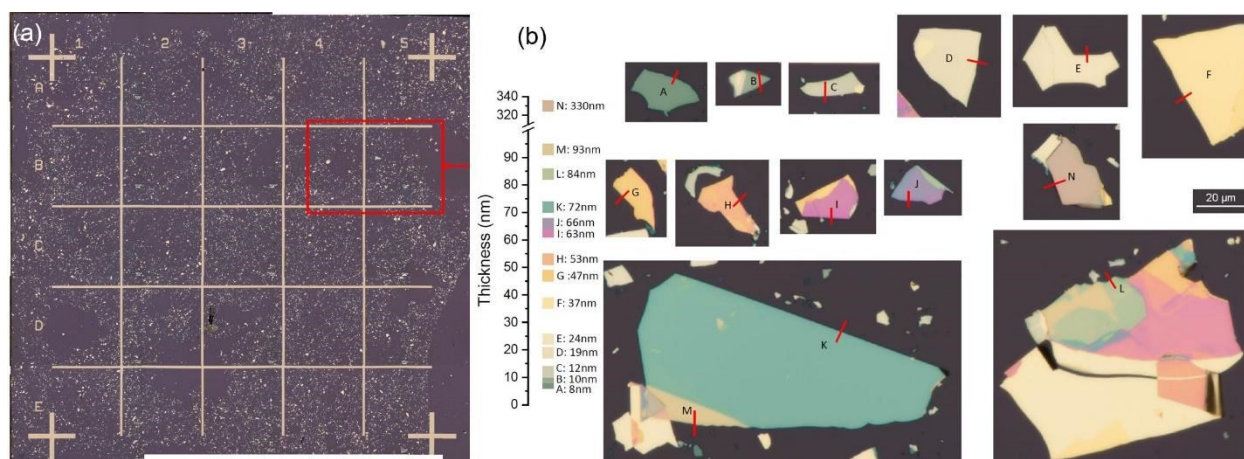


Figure S1.1. (a) Optical image of WS₂ flake exfoliated on a marked SiO₂/Si substrate. (b) Optical and AFM characterization of selected isolated WS₂ pristine flakes in the red rectangle area in (a). The color of the flake changes based on its thickness in the range of 8 – 340 nm.

Synthesis of Fe-implanted WS₂ flakes

Fe-implanted WS₂ samples were fabricated by a two-step mechanical exfoliation process of WS₂ onto a gold coated (Au (50 nm)/Ti (5 nm)) substrate with pre-patterned trenches and holes (~200 nm deep), see Figure S1.2. First, a bulk WS₂ piece is cleaved obtaining a flat and pristine surface, which rapidly gets pressed and thermal released onto the gold coated substrate. Mild annealing (150°C for 15 mins) is used to improve adhesion between the WS₂ and the gold surface. Second, the bulk WS₂ piece is removed with commercial low-residue tape, obtaining mainly mono- and few-layer WS₂ suspended over the trenches and holes. Suspended monolayer membranes were rapidly identified by fluorescence microscopy. Thicker suspended membranes were identified with optical contrast and AFM. Carbon tape conductive adhesive was placed on either side of the sample to separate the sample from the mask and to ensure proper charge dissipation of the ion's incident with the mask.

Hyperthermal Fe ions were implanted into some of the studied WS₂ flakes using a custom implanter^[58] based on a Colutron Ion Gun Model G-2-D with decelerator model 450 for use with ultralow energy ions down to 1 eV. A DC Ion Source with solid charge holder containing FeCl₂ as the Fe ion source precursor was used. Some of the studied WS₂ flakes were exposed to 4 nA (~1.2 nA/cm²) 30 eV Fe⁺ beams to a total Fe dose ranging from 1×10¹³ to 1×10¹⁴ Fe⁺/cm². To achieve regions with and without Fe⁺ exposure on the same flake, a metal shadow mask composed

of 127 μm holes on a hexagonal grid with a pitch of 220 μm was placed over the surface of the sample (Figure S1.2). Optical images were taken with the shadow mask present to determine the exposed regions of the samples based on the numbered alignment marks on the sample. Additionally, large area Raman maps (not shown here) were performed following implantation. These maps showed negligible change in the intensity for the ion implant doses imparted, yet the Raman modes have been shown to be more robust in TMD films than PL at low ion doses.^[59]

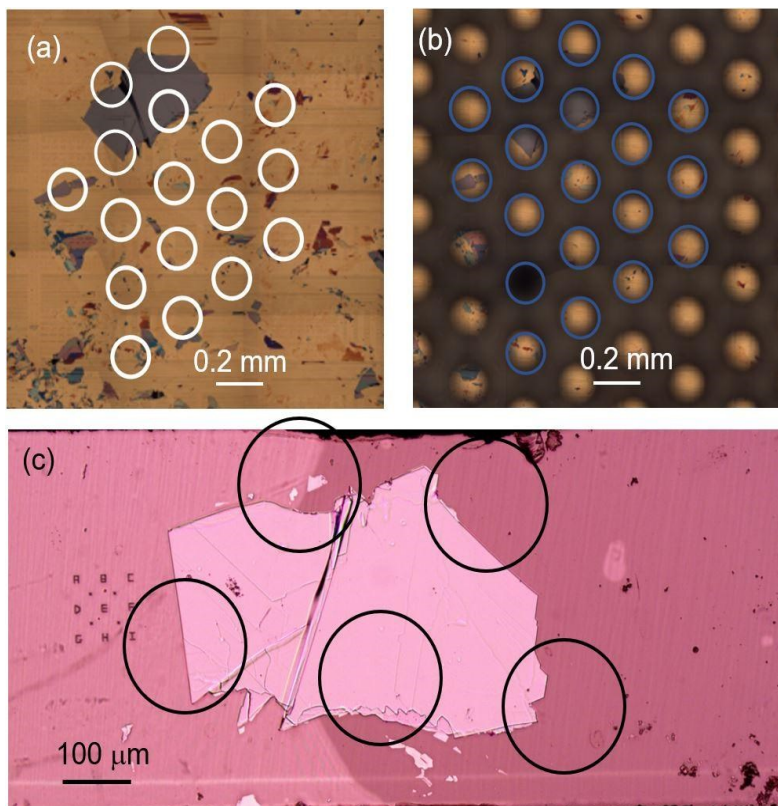


Figure S1.2. Optical image of a selected region with WS₂ flakes before (a) and after (b) depositing mask for ion beam implantation of Fe⁺ ions. The regions highlighted with circles show the places where Fe⁺ ions are being implanted. (c) Optical image of a pristine WS₂ flake transferred into a (110) diamond substance for NV measurements reported in the main manuscript and Supporting Information Section S3.

Transfer of WS₂ flakes into diamond substrates

WS₂ (pristine and/or Fe-implanted) flakes of interest were identified optically using standard optical color microscope^[60,61] and transferred to diamond substrates (see Figures S1.2c and S1.3c) using polypropylene carbonate (PPC) method (described in the main text).^[62,54] After transfer, any remaining PPC residue was cleaned off using anisole. We used hexagonal boron nitride (hBN) as a capping flake (thickness ~ 100 nm) on selected WS₂ flakes (see Figure S1.3(d-f) to prevent contamination during the transfer.^[63] Then, we resorted to nitrogen-vacancy (NV) magnetometry to image the magnetic stray field produced from pristine and Fe-implanted WS₂ flakes (thickness of 45 – 160 nm).

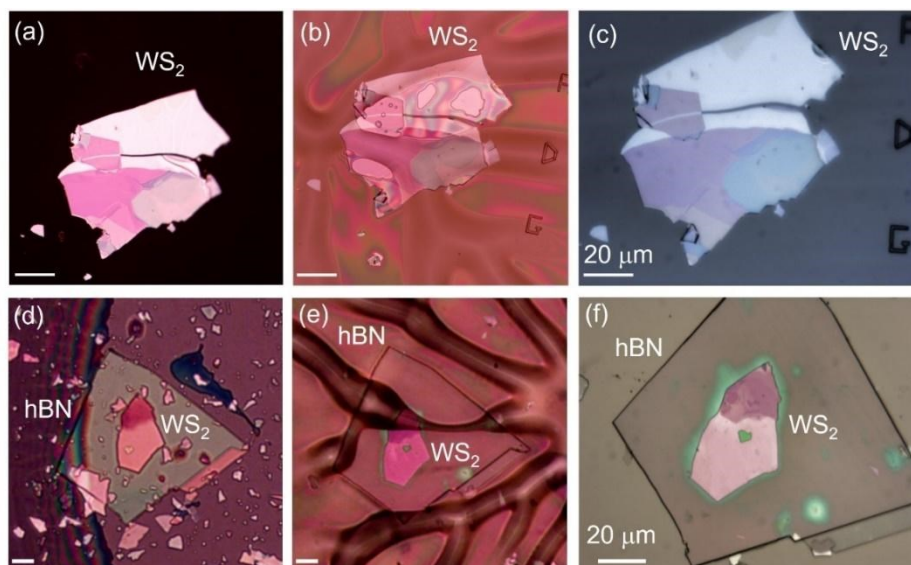


Figure S1.3. Optical images of a WS₂ flake on (a) a PPC stamp, (b) after being transferred onto the diamond substrate, and (c) after being cleaned with anisole. Optical image of a WS₂ flake (d) being transferred using a top layer of hBN on PPC, (e) after being transferred onto the diamond substrate, and (f) after being cleaned.

AFM measurements on WS₂ flakes transferred into diamond substrates

To measure the thickness of the WS₂ flakes transferred into the diamond substrates, we performed AFM measurements by using commercial AFM from Innova from Bruker.^[61] Figure S1.4a and Figure S1.4c show AFM maps of the WS₂ flakes transferred to (100) diamond. The flake thickness is determined from the step height in the line-cut profiles at the flake edge, see Figures S1.4b and S1.4d. The thickness of Flake 1 is ~160 nm, Flake 2 is ~100 nm, and Flake 3 is ~45 nm, respectively.

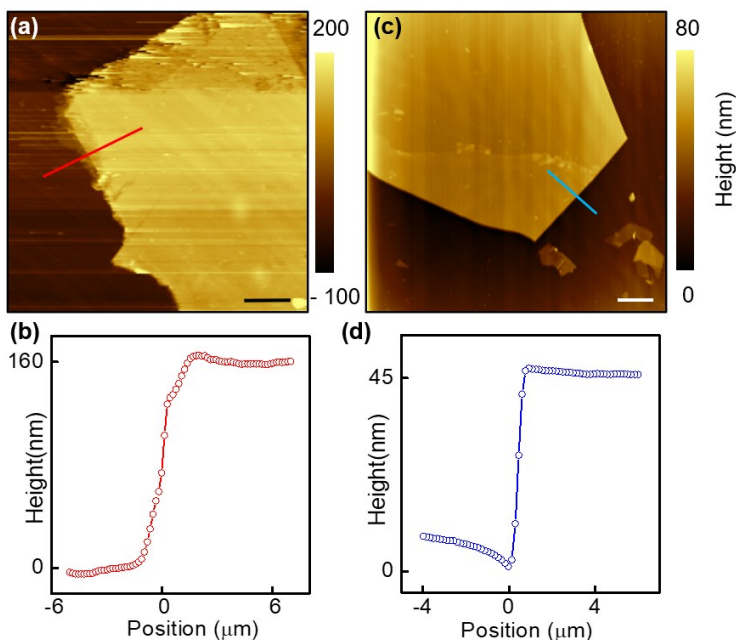


Figure S1.4. AFM image of WS₂ Flake 1 (a) and Flake 3 (c). (b) and (d) are the profiles of the flakes in (a) and (c) showing a height of ~160 nm and ~45 nm, respectively.

S2. Experimental Setup: optical detected magnetic resonance

Creation of NV centers in diamond

We used 2 mm × 2 mm × 0.5 mm type-IIa electronic grade (EL) (100) diamond (Element6) substrate with a nitrogen concentration < 5 ppb. The diamond is cut and polished along (100) and (110) planes at Delaware Diamond Knives Inc to 2 mm × 1 mm × 0.08 mm membranes. The diamond is then implanted at CuttingEdge Ions LLC with ¹⁵N ions. The (100) EL diamond is implanted with ¹⁵N ions at an energy of 4 keV and a dose of 1×10^{13} , similar to references [34,56]. The (110) diamond is implanted with ¹⁵N at four energies of 10, 20, 35, and 50 keV and four doses (1×10^{13} , 2×10^{13} , 3.5×10^{13} , and 5×10^{13} cm⁻²) respectively to create a uniform layer of NVs near the diamond surface.^[30,31] We used Stopping and Range of Ions in Matter (SRIM) Monte Carlo simulations to estimate the vacancy distribution depth profile in the diamond substrate and found a uniform distribution of vacancies within ~6 nm beneath (100) diamond (Figure S2a) and ~150 nm beneath (110) diamond (Figure S2b) facing the ¹⁵N ion source. After the implantation, the diamonds were annealed in a vacuum (pressure ~10⁻⁶ torr) at a temperature of 800 °C for 4 hours and 1100 °C for two hours and then cleaned for four hours in a 1:1:1 mixture of nitric, sulfuric, and perchloric acid at 200 °C to remove graphite residue at the surface.^[31,34,56] This process led in ~6-nm and ~150-nm NV layer near the surface with a density of ~1 ppm for (100)^[34,56] and ~10 ppm for (110)^[31] oriented diamond, respectively.

Optical magnetic resonance wide-field microscope.

To study the magnetic properties of WS₂ flakes, we used home-built wide-field optically detected magnetic resonance (ODMR) microscope, Figure S2(c-d). The ODMR microscope, described in detail in Reference [31], comprises a high NA (= 1.25) 100x oil immersion Nikon objective to focus the green laser (532 nm) with a laser of 130 mW, a dichroic mirror (DM, Semrock model FF560-FDi01) and a single-band bandpass filter (Semrock FF01-731-137) to collect the NV fluorescence (650 – 800 nm) and focus it on the sCMOS camera (Hamamatsu, ORCA-Flash4.0 V3) using a tube lens (Thorlabs, TTL200). To manipulate the $|m_s = 0\rangle \leftrightarrow |m_s = -1\rangle$ (f^-) and $|m_s = 0\rangle \leftrightarrow |m_s = +1\rangle$ (f^+) NV spin transitions, a microwave (MW) is provided by a signal generator (SRS: Stanford Research Systems, SG384) with two outputs for the main (DC-4 GHz) and double-frequency harmonic (4-8 GHz). It is then amplified by two MW amplifiers (Mini-Circuits ZHL-16W-43-s+ and ZVE-3W-83+) to achieve a MW power in the range of 100 mW – 10 W. The MW is then injected through Cu (1.5 μm)/Ti (5 nm) MW loops (width of 20 μm) patterned on a glass coverslip (thickness of 100 μm).

Permanent magnets (KJ magnetics, DX8X8-N52) were used to provide an external magnetic field, applied along the [111] direction in (100) and (110) diamonds. Figure S2c shows a picture of the ODMR wide-field microscope with a magnetic field of up to 100 mT along the [111] direction in (100) diamond. For (110) diamonds (Figure S2d), the magnetic field is contained within the plane of the diamond substrate and can reach an amplitude of 400 mT. To prevent from a strong field gradient across the wide-field fluorescence image 600 pixel × 600 pixel (up to 39 μm × 39 μm), we used two permanent magnets (DX8X8-N52) connected through stainless non-magnetic steel rods, see Figure S2d.^[31] To align the magnetic field along the NV [111] axis, a flip mirror is used to reflect the NV fluorescence and focus it with a lens (focal length of 30 mm) on an avalanche photon detector (APD, Thorlabs APD410A), connected to a Yokogawa oscilloscope (DL9041L). By monitoring the ODMR peaks in the oscilloscope along the [111] direction we can align the applied magnetic field very accurately. After the magnetic field alignment, the mirror is

flipped down and the NVs fluorescence is imaged by the sCMOS camera, and each MW frequency is swept along the f_- and f_+ NV spin transitions. More details for such measurements are provided in references [31,56].

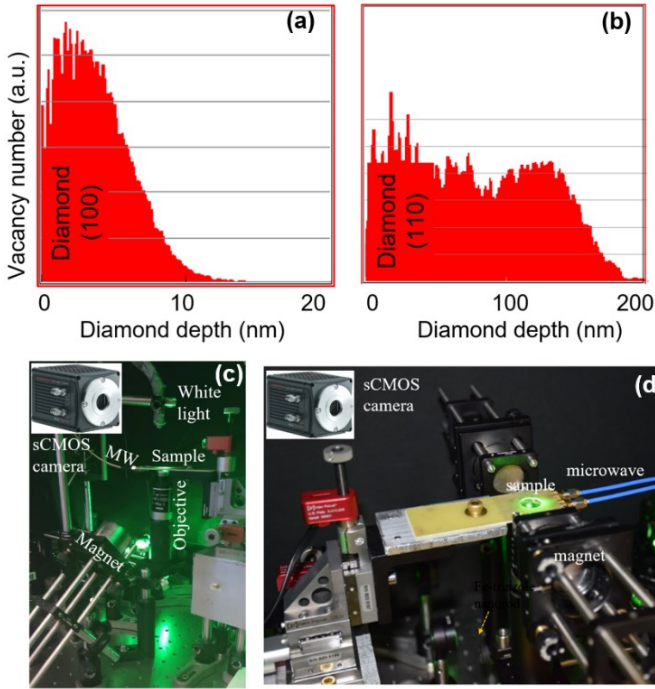


Figure S2. SRIM vacancy-depth profile for $^{15}\text{N}^+$ implantation in (100) diamond (a) and (110) diamond (b), corresponding to an NV layer of ~ 6 nm and ~ 150 nm, respectively. ODMR microscope integrated with a wide field sCMOS camera (upper inset) with magnetic field aligned along [111] in (100) diamond (c) and (110) diamond (d).

S3. Additional NV magnetometry measurements of WS_2 flakes

Figure S3.1a and Figure S3.1b show the NV normalized fluorescence and measured magnetic stray-field (B_{str}) maps at different values (4.4 – 63.1 mT) of the applied magnetic field B_{app} respectively, for the pristine WS_2 Flake 1 (thickness of ~ 160 nm) transferred into (100) diamond and studied in the main text.

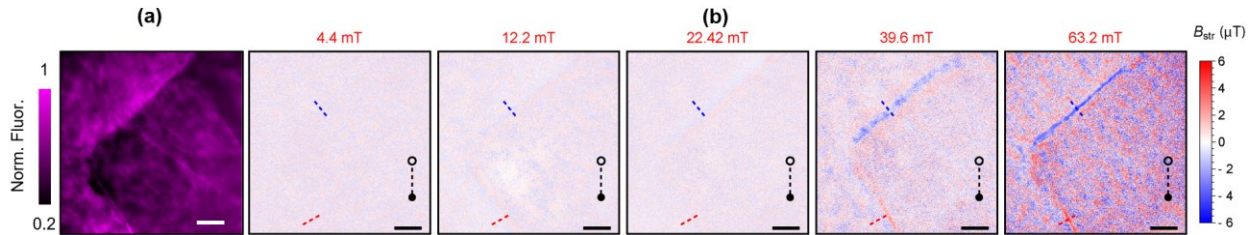


Figure S3.1. NV normalized fluorescence (a) and measured B_{str} (b) maps at different values of B_{app} (4.4 – 63.1 mT) for WS_2 Flake 1 transferred on (100) diamond. The scale bar is 5 μm .

Figure S3.2a and Figure S3.2b show the NV normalized fluorescence and measured B_{str} maps at different values (5.6 – 220 mT) of B_{app} , respectively, for pristine WS_2 Flake 2 (thickness of ~ 100 nm) transferred into (110) diamond and studied in the main text.

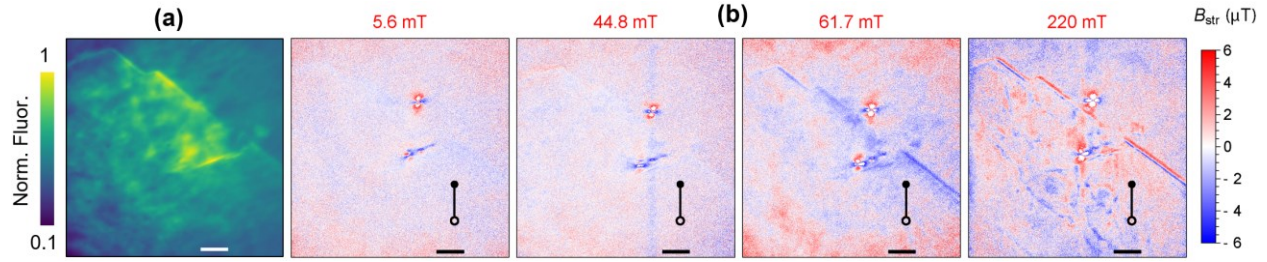


Figure S3.2. NV normalized fluorescence (a) and measured B_{str} (b) maps at different values of B_{app} (5.6 – 220 mT) for WS₂ Flake 2 transferred on (110) diamond. The scale bar is 5 μm .

Figure S3.3a and Figure S3.3b show the NV normalized fluorescence and measured B_{str} maps at different values (5.5 – 63.2 mT) of B_{app} , respectively, for pristine WS₂ Flake 3 (thickness of ~ 45 nm) transferred into (100) diamond and discussed in the main text.

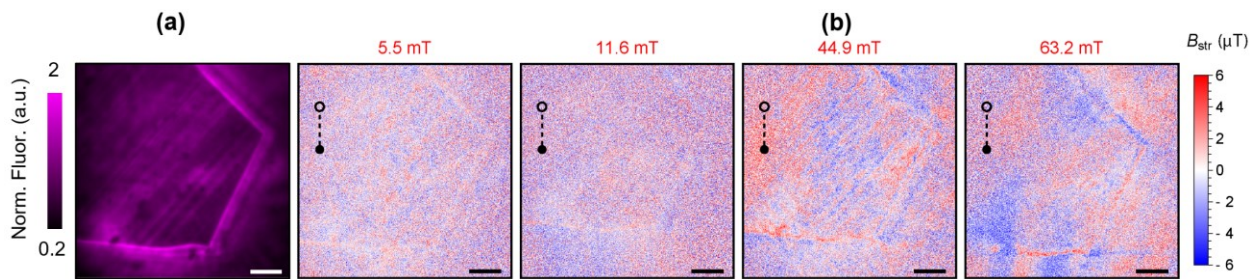


Figure S3.3. Normalized fluorescence map (a) and measured B_{str} maps (b) at different values of B_{app} (4.4 – 63.1 mT) for WS₂ Flake 3 transferred on (100) diamond. The scale bar is 5 μm .

Figure S3.4a and Figure S3.4b show the NV-measured and calculated B_{str} maps of pristine WS₂ Flake 3 (thickness of ~ 45 nm), respectively. Figure S3.4c and Figure S3.4d depict line cut profiles of the measured B_{str} at one (upper/lower) of Flake 1 (Figure S3.1) and Flake 3 edges at B_{app} of 63.2 mT, as indicated by the dashed blue and red lines in (a) and (b). See the main text for the comparison discussion between Flake 1 and Flake 3.

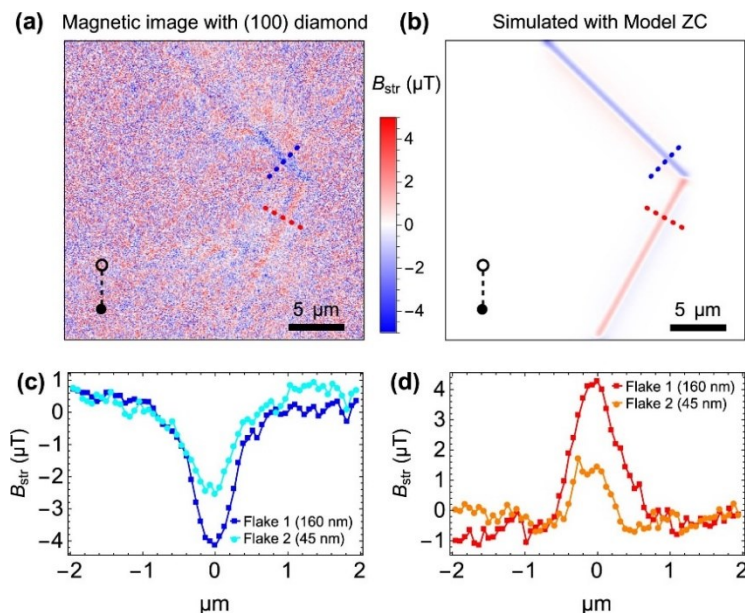


Figure S3.4. A measured (a) and simulated (b) B_{str} map of WS₂ Flake 3 transferred on (100) diamond at B_{app} of 63.2 mT. Line cuts of B_{str} across the edges of Flake 1 and Flake 3, corresponding to the blue (c) and red (d) curves for dashed lines in Figure 3b and Figure S3.4a, respectively, revealing field variations at different thicknesses.

S4. COMSOL model

Figure S4 illustrates the schematic of edge magnetization for the WS₂ flake (Flake 3) used in our COMSOL model, as detailed in Section 2.1 of the main text. The magnetic stray field is integrated over a finite-thickness layer corresponding to the NV layer in the diamond substrate. For clarity, the applied magnetic field (B_{app}), aligned with the NV axis, is depicted but not directly included in the COMSOL model. The WS₂ flake's edges are modeled as bars with sub-resolution cross-sectional dimensions, and magnetization (50–80 A/m) is assigned to the volumes of these bars.

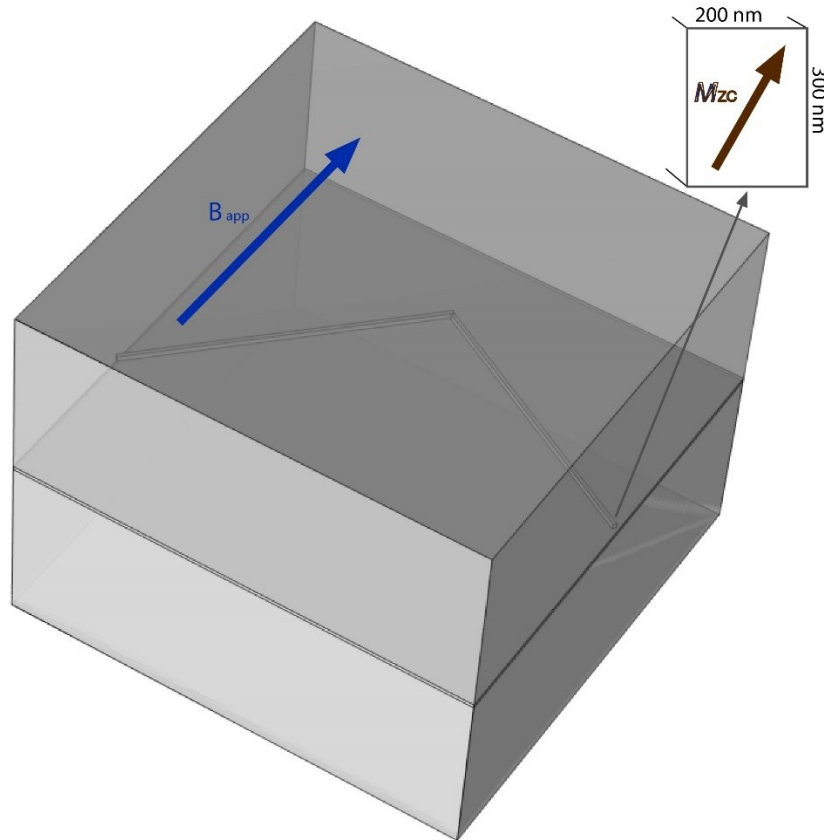


Figure S4. Schematic of the WS₂ flake (Flake 3) on a diamond substrate, illustrating the edge magnetization geometry used in the COMSOL model.

References

- [1] B. Huang, G. Clark, E. Navarro-Moratalla, D. R. Klein, R. Cheng, K. L. Seyler, D. Zhong, E. Schmidgall, M. A. McGuire, D. H. Cobden, W. Yao, D. Xiao, P. Jarillo-Herrero, X. Xu, *Nature* **2017**, *546*, 270.
- [2] C. Gong, L. Li, Z. Li, H. Ji, A. Stern, Y. Xia, T. Cao, W. Bao, C. Wang, Y. Wang, Z. Q. Qiu, R. J. Cava, S. G. Louie, J. Xia, X. Zhang, *Nature* **2017**, *546*, 265.
- [3] M. Bonilla, S. Kolekar, Y. Ma, H. C. Diaz, V. Kalappattil, R. Das, T. Eggers, H. R. Gutierrez, M.-H. Phan, M. Batzill, *Nature Nanotech* **2018**, *13*, 289.

- [4] Z. Fei, B. Huang, P. Malinowski, W. Wang, T. Song, J. Sanchez, W. Yao, D. Xiao, X. Zhu, A. F. May, W. Wu, D. H. Cobden, J.-H. Chu, X. Xu, *Nature Mater* **2018**, *17*, 778.
- [5] Y. Deng, Y. Yu, Y. Song, J. Zhang, N. Z. Wang, Z. Sun, Y. Yi, Y. Z. Wu, S. Wu, J. Zhu, J. Wang, X. H. Chen, Y. Zhang, *Nature* **2018**, *563*, 94.
- [6] S. N. Kajale, T. Nguyen, C. A. Chao, D. C. Bono, A. Boonkird, M. Li, D. Sarkar, *Nat Commun* **2024**, *15*, 1485.
- [7] Z. Fu, P. I. Samarawickrama, Y. Zhu, Z. Mao, W. Wang, K. Watanabe, T. Taniguchi, J. Tang, J. Ackerman, J. Tian, *Nano Lett.* **2023**, *23*, 11866.
- [8] Z. Fu, P. I. Samarawickrama, J. Ackerman, Y. Zhu, Z. Mao, K. Watanabe, T. Taniguchi, W. Wang, Y. Dahnovsky, M. Wu, T. Chien, J. Tang, A. H. MacDonald, H. Chen, J. Tian, *Nat Commun* **2024**, *15*, 3630.
- [9] X.-L. Fan, Y.-R. An, W.-J. Guo, *Nanoscale Res Lett* **2016**, *11*, 154.
- [10] J. Wang, J. Kang, S. Chyczewski, Y. Lin, H. Lee, W. Zhu, X. Hong, *J. Phys. D: Appl. Phys.* **2025**, *58*, 063001.
- [11] P. Liu, Y. Zhang, K. Li, Y. Li, Y. Pu, *iScience* **2023**, *26*, 107584.
- [12] L. Cai, J. He, Q. Liu, T. Yao, L. Chen, W. Yan, F. Hu, Y. Jiang, Y. Zhao, T. Hu, Z. Sun, S. Wei, *J. Am. Chem. Soc.* **2015**, *137*, 2622.
- [13] F. Zhang, B. Zheng, A. Sebastian, D. H. Olson, M. Liu, K. Fujisawa, Y. T. H. Pham, V. O. Jimenez, V. Kalappattil, L. Miao, T. Zhang, R. Pendurthi, Y. Lei, A. L. Elías, Y. Wang, N. Alem, P. E. Hopkins, S. Das, V. H. Crespi, M.-H. Phan, M. Terrones, *Advanced Science* **2020**, *7*, 2001174.
- [14] S. Fu, K. Kang, K. Shayan, A. Yoshimura, S. Dadras, X. Wang, L. Zhang, S. Chen, N. Liu, A. Jindal, X. Li, A. N. Pasupathy, A. N. Vamivakas, V. Meunier, S. Strauf, E.-H. Yang, *Nat Commun* **2020**, *11*, 2034.
- [15] W. Yu, J. Li, T. S. Heng, Z. Wang, X. Zhao, X. Chi, W. Fu, I. Abdelwahab, J. Zhou, J. Dan, Z. Chen, Z. Chen, Z. Li, J. Lu, S. J. Pennycook, Y. P. Feng, J. Ding, K. P. Loh, *Adv. Mater.* **2019**, *31*, 1903779.
- [16] S. J. Yun, D. L. Duong, D. M. Ha, K. Singh, T. L. Phan, W. Choi, Y. Kim, Y. H. Lee, *Advanced Science* **2020**, *7*, 1903076.
- [17] R. Mishra, W. Zhou, S. J. Pennycook, S. T. Pantelides, J.-C. Idrobo, *Phys. Rev. B* **2013**, *88*, 144409.
- [18] X. Lin, J. Ni, *Journal of Applied Physics* **2014**, *116*, 044311.
- [19] J. Wang, F. Sun, S. Yang, Y. Li, C. Zhao, M. Xu, Y. Zhang, H. Zeng, *Applied Physics Letters* **2016**, *109*, 092401.
- [20] S. Ahmed, X. Ding, P. P. Murmu, N. Bao, R. Liu, J. Kennedy, L. Wang, J. Ding, T. Wu, A. Vinu, J. Yi, *Small* **2020**, *16*, 1903173.
- [21] S. Ahmed, X. Ding, N. Bao, P. Bian, R. Zheng, Y. Wang, P. P. Murmu, J. V. Kennedy, R. Liu, H. Fan, K. Suzuki, J. Ding, J. Yi, *Chem. Mater.* **2017**, *29*, 9066.
- [22] M. Habib, Z. Muhammad, R. Khan, C. Wu, Z. Ur Rehman, Y. Zhou, H. Liu, L. Song, *Nanotechnology* **2018**, *29*, 115701.
- [23] B. Xia, Q. Guo, D. Gao, S. Shi, K. Tao, *J. Phys. D: Appl. Phys.* **2016**, *49*, 165003.
- [24] J. Luo, C. Li, J. Liu, Y. Liu, W. Xiao, R. Zheng, Q. Zheng, J. Han, T. Zou, W. Cheng, X. Yao, Y. Liu, J. Zhu, *Applied Physics Letters* **2024**, *124*, 033104.
- [25] B. Han, F. Li, L. Li, X. Huang, Y. Gong, X. Fu, H. Gao, Q. Zhou, T. Cui, *J. Phys. Chem. Lett.* **2017**, *8*, 941.
- [26] X. Mao, Y. Xu, Q. Xue, W. Wang, D. Gao, *Nanoscale Res Lett* **2013**, *8*, 430.

- [27] J. Luxa, O. Jankovský, D. Sedmidubský, R. Medlín, M. Maryško, M. Pumera, Z. Sofer, *Nanoscale* **2016**, *8*, 1960.
- [28] N. Huo, Y. Li, J. Kang, R. Li, Q. Xia, J. Li, *Applied Physics Letters* **2014**, *104*, 202406.
- [29] K. Kang, S. Fu, K. Shayan, Y. Anthony, S. Dadras, X. Yuzan, F. Kazunori, M. Terrones, W. Zhang, S. Strauf, V. Meunier, A. N. Vamivakas, E.-H. Yang, *Nanotechnology* **2021**, *32*, 095708.
- [30] I. Fescenko, A. Laraoui, J. Smits, N. Mosavian, P. Kehayias, J. Seto, L. Bougas, A. Jarmola, V. M. Acosta, *Phys. Rev. Appl.* **2019**, *11*, 034029.
- [31] S. Lamichhane, K. A. McElveen, A. Erickson, I. Fescenko, S. Sun, R. Timalsina, Y. Guo, S.-H. Liou, R. Y. Lai, A. Laraoui, *ACS Nano* **2023**, *17*, 8694.
- [32] A. Laraoui, K. Ambal, *Applied Physics Letters* **2022**, *121*, 060502.
- [33] A. Erickson, S. Q. Abbas Shah, A. Mahmood, I. Fescenko, R. Timalsina, C. Binek, A. Laraoui, *RSC Adv.* **2023**, *13*, 178.
- [34] R. Timalsina, H. Wang, B. Giri, A. Erickson, X. Xu, A. Laraoui, *Adv Elect Materials* **2024**, *10*, 2300648.
- [35] A. Erickson, S. Q. A. Shah, A. Mahmood, P. Buragohain, I. Fescenko, A. Gruverman, C. Binek, A. Laraoui, *Adv Funct Materials* **2024**, 2408542.
- [36] A. Erickson, Q. Zhang, H. Vakili, C. Li, S. Sarin, S. Lamichhane, L. Jia, I. Fescenko, E. Schwartz, S.-H. Liou, J. E. Shield, G. Chai, A. A. Kovalev, J. Chen, A. Laraoui, *ACS Nano* **2024**, *18*, 31261.
- [37] A. Berzins, J. Smits, A. Petruhins, R. Rimisa, G. Mozolevskis, M. Zubkins, I. Fescenko, *Opt. Express* **2023**, *31*, 17950.
- [38] L. Thiel, Z. Wang, M. A. Tschudin, D. Rohner, I. Gutiérrez-Lezama, N. Ubrig, M. Gibertini, E. Giannini, A. F. Morpurgo, P. Maletinsky, *Science* **2019**, *364*, 973.
- [39] F. Fabre, A. Finco, A. Purbawati, A. Hadj-Azzem, N. Rougemaille, J. Coraux, I. Philip, V. Jacques, *Phys. Rev. Materials* **2021**, *5*, 034008.
- [40] T. Song, Q.-C. Sun, E. Anderson, C. Wang, J. Qian, T. Taniguchi, K. Watanabe, M. A. McGuire, R. Stöhr, D. Xiao, T. Cao, J. Wrachtrup, X. Xu, *Science* **2021**, *374*, 1140.
- [41] Q.-C. Sun, T. Song, E. Anderson, A. Brunner, J. Förster, T. Shalomayeva, T. Taniguchi, K. Watanabe, J. Gräfe, R. Stöhr, X. Xu, J. Wrachtrup, *Nat Commun* **2021**, *12*, 1989.
- [42] E. Marchiori, L. Ceccarelli, N. Rossi, L. Lorenzelli, C. L. Degen, M. Poggio, *Nat Rev Phys* **2021**, *4*, 49.
- [43] M. A. Tschudin, D. A. Broadway, P. Siegwolf, C. Schrader, E. J. Telford, B. Gross, J. Cox, A. E. E. Dubois, D. G. Chica, R. Rama-Eiroa, E. J. G. Santos, M. Poggio, M. E. Ziebel, C. R. Dean, X. Roy, P. Maletinsky, *Nat Commun* **2024**, *15*, 6005.
- [44] X. Li, A. C. Jones, J. Choi, H. Zhao, V. Chandrasekaran, M. T. Pettes, A. Piryatinski, M. A. Tschudin, P. Reiser, D. A. Broadway, P. Maletinsky, N. Sinitsyn, S. A. Crooker, H. Htoon, *Nat. Mater.* **2023**, *22*, 1311.
- [45] X.-Y. Zhang, Y.-X. Wang, T. A. Tartaglia, T. Ding, M. J. Gray, K. S. Burch, F. Tafti, B. B. Zhou, *PRX Quantum* **2021**, *2*, 030352.
- [46] M. W. Doherty, N. B. Manson, P. Delaney, F. Jelezko, J. Wrachtrup, L. C. L. Hollenberg, *Physics Reports* **2013**, *528*, 1.
- [47] C. Liu, G. Zhao, S. Picozzi, X. Li, J. Yang, *Phys. Rev. B* **2024**, *110*, 094409.
- [48] N. V. Proscia, Z. Shotan, H. Jayakumar, P. Reddy, C. Cohen, M. Dollar, A. Alkauskas, M. Doherty, C. A. Meriles, V. M. Menon, *Optica* **2018**, *5*, 1128.

- [49] S. W. LaGasse, N. V. Proscia, C. D. Cress, J. J. Fonseca, P. D. Cunningham, E. Janzen, J. H. Edgar, D. J. Pennachio, J. Culbertson, M. Zalalutdinov, J. T. Robinson, *Advanced Materials* **2024**, *36*, 2309777.
- [50] X. Ding, T. Liu, S. Ahmed, N. Bao, J. Ding, J. Yi, *Journal of Alloys and Compounds* **2019**, *772*, 740.
- [51] P. Maletinsky, S. Hong, M. S. Grinolds, B. Hausmann, M. D. Lukin, R. L. Walsworth, M. Loncar, A. Yacoby, *Nature Nanotech* **2012**, *7*, 320.
- [52] B. Zhang, P. Lu, R. Tabrizian, P. X.-L. Feng, Y. Wu, *npj Spintronics* **2024**, *2*, 6.
- [53] F. M. O. Brito, L. Li, J. M. V. P. Lopes, E. V. Castro, *Phys. Rev. B* **2022**, *105*, 195130.
- [54] K. Kinoshita, R. Moriya, M. Onodera, Y. Wakafuji, S. Masubuchi, K. Watanabe, T. Taniguchi, T. Machida, *npj 2D Mater Appl* **2019**, *3*, 1.
- [55] R. Frisenda, E. Navarro-Moratalla, P. Gant, D. P. D. Lara, P. Jarillo-Herrero, R. V. Gorbachev, A. Castellanos-Gomez, *Chem. Soc. Rev.* **2018**, *47*, 53.
- [56] S. Lamichhane, R. Timalina, C. Schultz, I. Fescenko, K. Ambal, S.-H. Liou, R. Y. Lai, A. Laraoui, *Nano Lett.* **2024**, *24*, 873.
- [57] I. Fescenko, **2023**, DOI 10.48550/ARXIV.2303.12544.
- [58] C. D. Cress, S. W. Schmucker, A. L. Friedman, P. Dev, J. C. Culbertson, J. W. Lyding, J. T. Robinson, *ACS Nano* **2016**, *10*, 3714.
- [59] J. Klein, A. Kuc, A. Nolinder, M. Altschner, J. Wierzbowski, F. Sigger, F. Kreupl, J. J. Finley, U. Wurstbauer, A. W. Holleitner, M. Kaniber, *2D Mater.* **2017**, *5*, 011007.
- [60] M. Dowran, A. Butler, S. Lamichhane, A. Erickson, U. Kilic, S. Liou, C. Argyropoulos, A. Laraoui, *Advanced Optical Materials* **2023**, *11*, 2300392.
- [61] M. Dowran, U. Kilic, S. Lamichhane, A. Erickson, J. Barker, M. Schubert, S. Liou, C. Argyropoulos, A. Laraoui, *Laser & Photonics Reviews* **2025**, *19*, 2400705.
- [62] F. Pizzocchero, L. Gammelgaard, B. S. Jessen, J. M. Caridad, L. Wang, J. Hone, P. Bøggild, T. J. Booth, *Nat Commun* **2016**, *7*, 11894.
- [63] S. Fukamachi, P. Solís-Fernández, K. Kawahara, D. Tanaka, T. Otake, Y.-C. Lin, K. Suenaga, H. Ago, *Nat Electron* **2023**, *6*, 126.